ELSEVIER

Effects of spanwise rotation on the vorticity stretching in transitional and turbulent channel flow

Eric Lamballais, Marcel Lesieur, and Olivier Métais

Laboratoire des Ecoulements Géophysiques et Industriels, UMR CNRS 5519 Institut de Mécanique de Grenoble, Institut National Polytechnique et Université Joseph Fourier, Grenoble, France

We investigate, by means of direct numerical simulations, the three-dimensional (3-D) dynamics of coherent vortices in a rotating channel. We focus here on the structure of the instantaneous (absolute and relative) vorticity field. Both transitional and turbulent regimes are considered. Strong rotation is shown to suppress the transition towards turbulence (leading to two-dimensional [2-D] flow). Conversely, moderate rotation yields strong longitudinal vortices on the anticyclonic side of the channel, which trigger early transition (earlier than without rotation). In that regime, the complete transition to fully developed turbulence is compared for two values of Rossby number: $|\mathrm{Ro}^{(i)}|=2$ and $|\mathrm{Ro}^{(i)}|=6$. In the early stage of the transition, perturbations are more strongly amplified at $|\mathrm{Ro}^{(i)}|=2$. The saturation is, however, reached earlier in that case, and a more energetic turbulent state is achieved at $|\mathrm{Ro}^{(i)}|=6$. In the fully developed turbulent case, nonrotating and moderately rotating channels are compared. Relaminarization occurs on the cyclonic wall, while turbulence is observed on the anticyclonic wall. The vortex topology is shown to be strongly affected by the rotation. The enhancement of the anticyclonic perturbations level is associated with hairpin vortices which are much more inclined (up to 10° to the wall) than in the nonrotating case (45°). These extend until the channel center and are associated with a characteristic region of zero absolute mean vorticity. Stretching mechanisms of absolute vortex lines are carefully examined.

Introduction

We investigate, via three-dimensional (3-D) direct numerical simulations (DNSs), the influence of spanwise rotation on transitional and turbulent channel flow (Figure 1).

Because of their engineering applications for turbomachinery, several laboratory experiments have focused on rotating bounded flows, such as boundary layers over flat surfaces and flow in a straight channel. Several basic features of the boundary layers over rotating solid surfaces have been determined. Let $\bar{\mathbf{u}} = (\bar{u}(y),0,0)$ be the mean velocity (x is in the streamwise direction and y in the direction perpendicular to the wall). The rotation vector $\boldsymbol{\Omega} = (0,0,\Omega)$ is oriented along the spanwise direction z and may be positive or negative. For the channel flow, the vorticity vector associated with the mean velocity profile $\bar{\boldsymbol{\omega}} = (0,0,-d\bar{u}/dy)$ is parallel to $\boldsymbol{\Omega}$ near one wall and antiparallel near the opposite wall; we refer to flow near these two particular walls as cyclonic and anticyclonic, respectively. Various other terms are used. The names suction and pressure sides originate from the pressure gradient due to the Coriolis force, and the terms trailing and leading sides are borrowed from the turbomachinery literature.

The parameter characterizing the rotation strength is the local Rossby number defined as

$$\mathrm{Ro}(y) = -\frac{d\bar{u}}{dy}\Big/2\Omega \tag{1}$$

The laboratory experiments have shown that the cyclonic side is stabilized; as compared to the nonrotating case, the turbulence energy production decreases with increasing rotation rate, and fast rotation can lead to the total suppression of turbulent transition. Conversely, the anticyclonic side is destabilized for moderate rotation rates (high enough Rossby numbers). Numerical simulations of rotating channel flows (Kim 1983; Tafti and Vanka 1991; Kristoffersen and Andersson 1993; Piomelli and Liu 1995) have complemented the experimental investigations. No experimental or numerical data seem to be available for high-rotation rates.

Address reprint requests to Dr. O. Métais, Laboratoire des Ecoulements Géophysiques et Industriels, Institut de Mécanique de Grenoble, Institut National Polytechnique et Université Joseph Fourier, B. P. 53, 38041, Grenoble Cedex 9, France.

Received 27 October 1995; accepted 10 February 1996

Int. J. Heat and Fluid Flow 17: 324–332, 1996

655 Avenue of the Americas, New York, NY 10010

0142-727X/96/$15.00
PII S0142-727X(96)00043-0

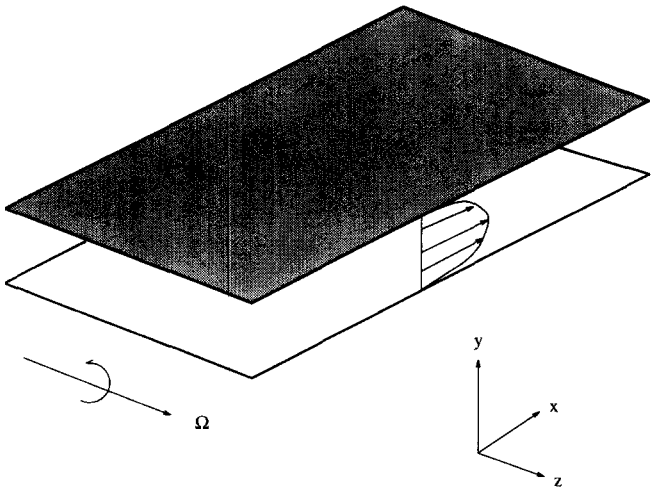

Figure 1 Schematic of the spanwise rotating channel flow problem

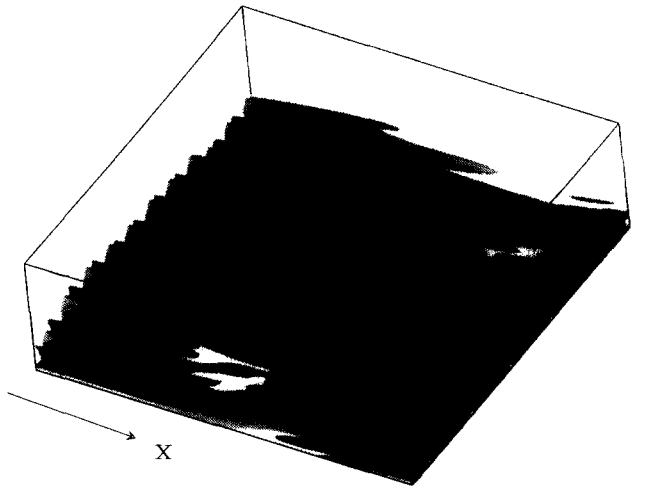

Figure 3 Isosurfaces of the longitudinal vorticity $\omega_x = \pm 0.75$ at $|Ro^{(i)}| = 6$, $Re = 8000$, $t = 28$

For free-shear flows, the drastically different effects of solid-body rotation, depending on whether the sense of rotation is cyclonic or anticyclonic, have been investigated in several laboratory and numerical experiments. Numerical investigation of planar mixing layers and wakes submitted to solid-body rotation of axis parallel to the basic vorticity have been performed by Lesieur et al. (1991) and Métais et al. (1995). They have shown that, for small Rossby numbers, the rotation renders the flow more two-dimensional (2-D) both in the cyclonic and anticyclonic cases. At moderate anticyclonic rotation rates, a critical value of the Rossby number was found for which the flow is strongly destabilized. The flow three-dimensionalization, in that case, is due to an intense stretching of the *absolute* vortex lines yielding intense longitudinal absolute hairpin vortices. Furthermore, it was checked that maximum stretching takes place in regions where the local Rossby number is close to unity, in agreement with the phenomenological theory proposed by Lesieur et al. Our purpose here is to investigate if similar observations can be made in the rotating channel flow.

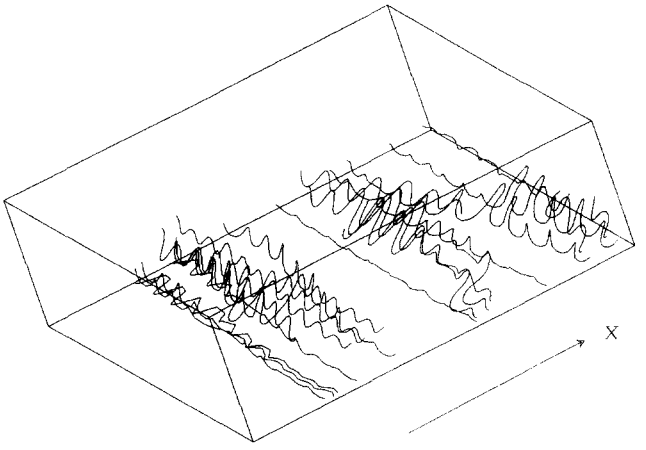

Figure 4 Absolute vortex filaments at $|Ro^{(i)}| = 6$, $Re = 8000$, $t = 28$

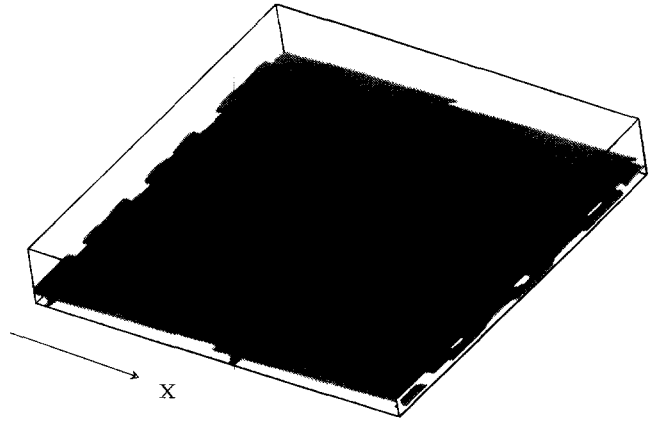

Figure 2 Isosurface of the vorticity modulus $\omega = 1.5$ at $|Ro^{(i)}| = \infty$, $Re = 8000$, $t = 3430$ (only the lower half of the channel is presented)

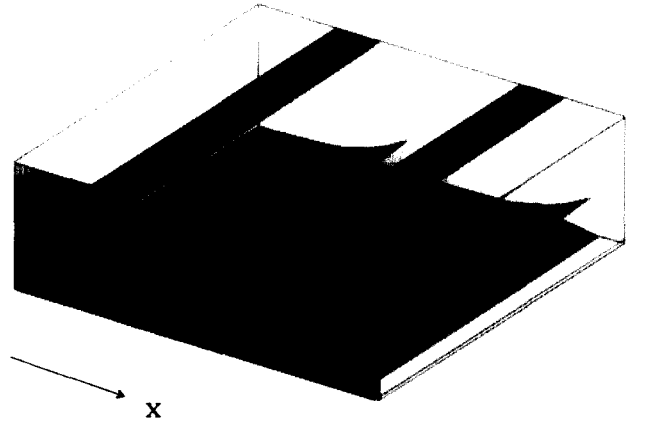

Figure 5 Isosurface of the spanwise vorticity $\omega_z = -1.5$-spanwise vorticity map for $z = 0$ at $|Ro^{(i)}| = 0.1$, $Re = 8000$, $t > 4000$

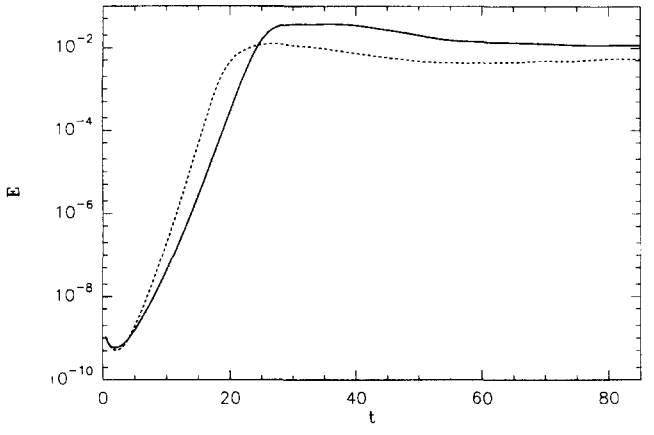

Figure 6 Temporal evolution of the fluctuating energy: ——, $|Ro^{(i)}|=6$; ···, $|Ro^{(i)}|=2$ (Re=3750)

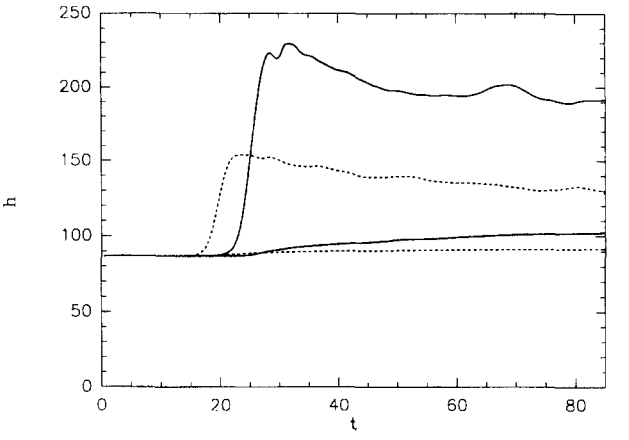

Figure 7 Temporal evolution of the half-channel width normalized with cyclonic or anticyclonic friction velocity and the viscosity ν, respectively h_c^+ and h_a^+. ——, $|Ro^{(i)}|=6$; ···, $|Ro^{(i)}|=2$; lower curves, h_c^+; upper curves; h_a^+ (Re=3750)

Numerical aspects

In a reference frame rotating at a constant angular velocity Ω, the incompressible Navier–Stokes equations can be written as:

$$\frac{\partial \mathbf{u}}{\partial t} + (\boldsymbol{\omega} + 2\boldsymbol{\Omega}) \times \mathbf{u} = -\frac{1}{\rho}\boldsymbol{\nabla}\pi + \nu\boldsymbol{\nabla}^2\mathbf{u} \tag{2}$$

$$\boldsymbol{\nabla} \cdot \mathbf{u} = 0 \tag{3}$$

$\mathbf{u} = (u, v, w)$, $\boldsymbol{\omega} = (\omega_x, \omega_y, \omega_z)$ and $\boldsymbol{\Omega} = (0, 0, \Omega)$ are, respectively, the relative velocity, relative vorticity, and rotation vectors. π is the modified pressure, including the (conservative) centrifugal force. $\boldsymbol{\omega}_a = \boldsymbol{\omega} + 2\boldsymbol{\Omega}$ will designate the absolute vorticity.

A detailed analysis of the 3-D flow structures requires high-order numerical schemes. We have then developed a numerical code solving the incompressible 3-D Navier–Stokes equations combining pseudospectral methods in the periodicity directions (streamwise and spanwise directions) and high-order finite difference schemes in the direction normal to the wall. Sixth-order compact differences schemes are used (see Lele 1992) with a stretched mesh. Velocity and pressure are discretized on the same grid. Note that the spurious oscillations in π, which are characteristic of the nonstaggered grids, are minimized due to the accuracy of the compact schemes (see Shih et al. 1989). For time discretization, a Crank–Nicholson scheme is used for the viscous term and a third-order Runge–Kutta scheme for the remaining. A fractional step method is adopted to ensure incompressibility. In the resolution of the Poisson equation, the computations of the various operators is such that the velocity field satisfies the divergence-free condition up to machine accuracy in the whole calculation domain.

Both for the transitional and turbulent channel flows, excellent comparisons have been obtained with the results of Zang and Krist (1989) and Kim et al. (1987) based on spectral methods. Comparable resolution is here used confirming the "spectral-like accuracy" of the compact schemes.

Transitional flow

Early transition

The initial conditions correspond to a basic Poiseuille velocity profile to which is superimposed a small-amplitude random perturbation (three-dimensional white noise) of intensity $\approx 10^{-4}U_c$, where U_c is the centerline velocity of the parabolic profile. The present computations have been performed with a constant mass flux. The Reynolds number Re is here chosen equal to 8000, (where Re is based on U_c and half-channel height h) so that the parabolic profile is unstable to small perturbations in the nonrotating case. Notice that, in the previous studies by Alfredsson and Persson (1989), Finlay (1990, 1992), Yang and Kim (1991), the Reynolds numbers was insufficient to have subcritical or supercritical transition without rotation. Throughout this paper, we

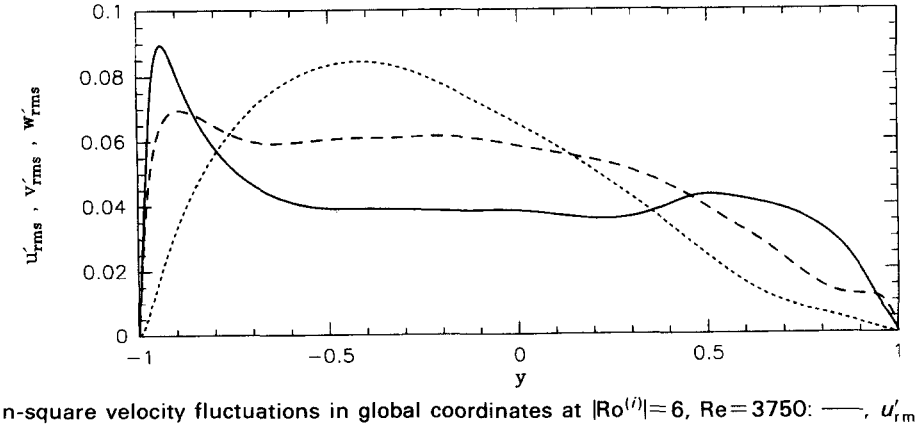

Figure 8 Root-mean-square velocity fluctuations in global coordinates at $|Ro^{(i)}|=6$, Re=3750: ——, u'_{rms}; ···, v'_{rms}; - - -, w'_{rms}

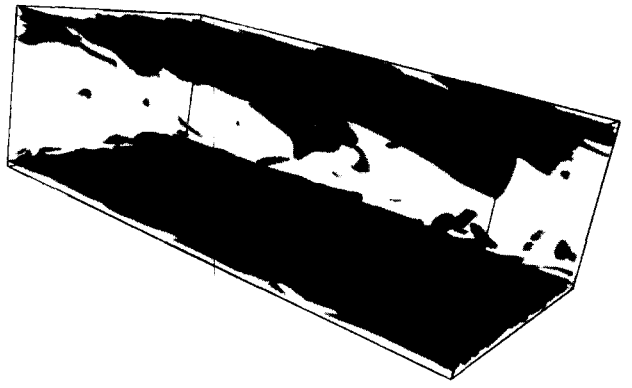

Figure 9 Isosurface of the vorticity modulus $\omega=3$ at $|\mathrm{Ro}^{(i)}|=\infty$, $\mathrm{Re}=3750$

use the normalization $U_c = 1$ and $h = 1$. Let $|\mathrm{Ro}^{(i)}|$ be the Rossby number associated with the vorticity maxima of the initial basic velocity profile. We compare three direct numerical simulations of transition at different Rossby numbers: $|\mathrm{Ro}^{(i)}| = 0.1, 2, 6, \infty$ where $|\mathrm{Ro}^{(i)}| = \infty$ denotes the case without notation. The size of the computational domain is $(L_x, L_y, L_z) = (4\pi, 2, 4\pi)$. The streamwise length is equal to twice the most amplified 2-D wavelength predicted by the linear stability analysis (Tollmien–Schlichting mode). The spanwise length is large enough to allow for several Λ-shaped vortices to appear (Figure 2).

Simulations are started on a coarse grid ($14 \times 97 \times 26$) which is progressively refined in the periodicity directions. The final grid is ($192 \times 97 \times 26$) for $|\mathrm{Ro}^{(i)}| = 0.1$, ($90 \times 97 \times 240$) for $|\mathrm{Ro}^{(i)}| = 6$ and 2, ($64 \times 97 \times 192$) for $|\mathrm{Ro}^{(i)}| = \infty$.

$|\mathrm{Ro}^{(i)}|=\infty$. Previous results are covered here (Zang and Krist 1989). The initial stage is dominated by the growth of 2-D Tollmien–Schlichting waves. They become unstable to 3-D perturbations when their amplitude exceeds a critical threshold. Λ-shaped vortices then form with a characteristic vortical pattern shown in Figure 2. Only aligned vortices are present, because, in the absence of external forcing, they constitute the most probable pattern (Kim and Moser 1989).

Moderate rotation: $|\mathrm{Ro}^{(i)}|=6$ and $|\mathrm{Ro}^{(i)}|=2$. As compared with the nonrotating case, the transition occurs earlier on the anticyclonic side of the channel. At these Rossby numbers, the most amplified mode is a purely longitudinal mode without streamwise dependence ($k_x = 0$). However, as noted by Yang and Kim (1991), 3-D waves with small k_x exhibit comparable growth

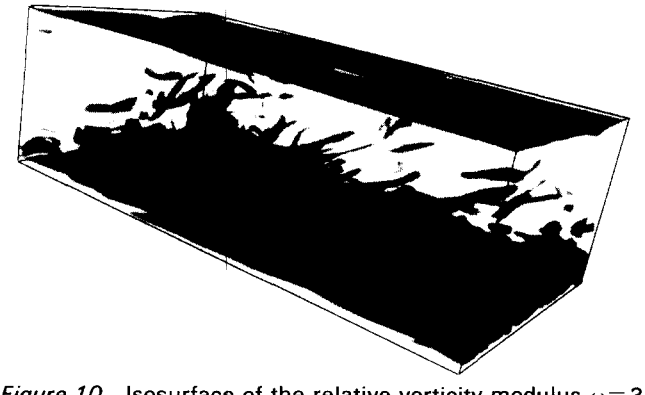

Figure 10 Isosurface of the relative vorticity modulus $\omega=3$ at $|\mathrm{Ro}^{(i)}|=6$, $\mathrm{Re}=3750$

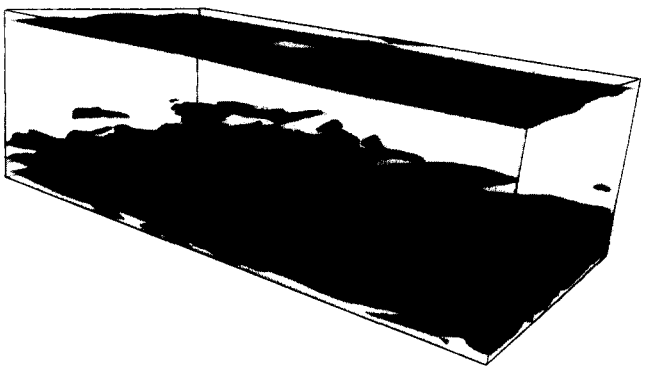

Figure 11 Isosurface of the relative vorticity modulus $\omega=2$ at $|\mathrm{Ro}^{(i)}|=2$, $\mathrm{Re}=3750$

rates. Similar results were found for rotating free-shear flows by Métais et al. (1995). Isosurfaces of longitudinal vorticity show counterrotating vortices oriented along the streamwise direction. These emerge in the early nonlinear stage (at $t = 28$ for $|\mathrm{Ro}^{(i)}| = 6$, see Figure 3). For $|\mathrm{Ro}^{(i)}| = 2$, the initial perturbation growth is

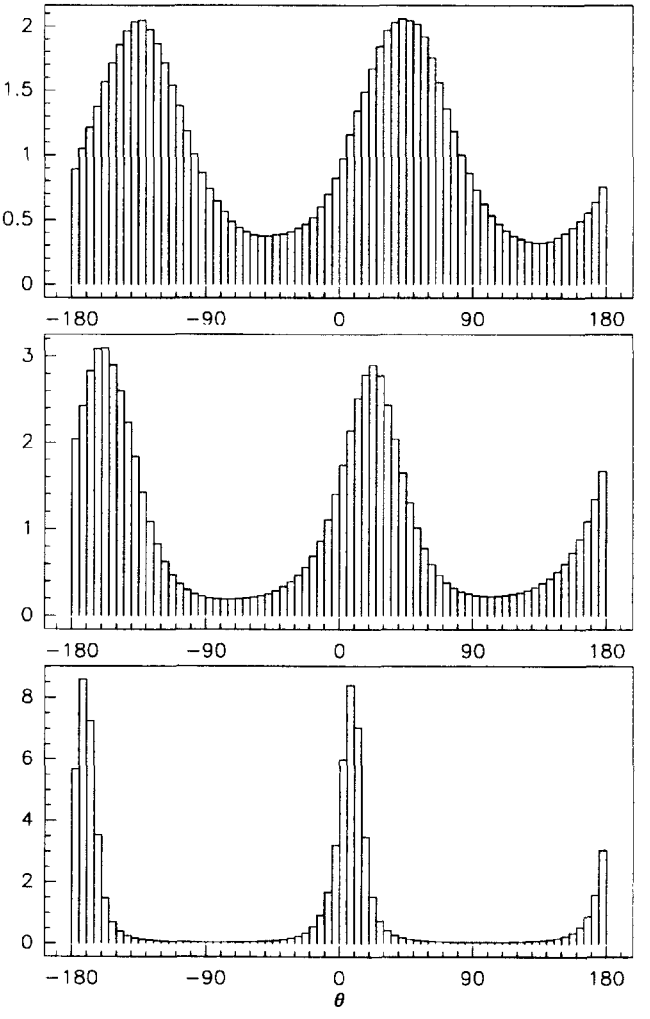

Figure 12 Distribution of the inclination of the projection of the vorticity vectors in (x, y)-planes; data weighted with the magnitude of the projected vorticity; $y = -0.5$, upper figure: $|\mathrm{Ro}^{(i)}|=\infty$ middle figure: $|\mathrm{Ro}^{(i)}|=6$ lower figure: $|\mathrm{Ro}^{(i)}|=2$ ($\mathrm{Re}=3750$)

higher, and these longitudinal vortices are formed earlier. This is in agreement with the predictions performed by Yanase et al. (1993) on the basis of a simplified form of the generalized Orr–Sommerfeld equations: in the limit of $Re \to \infty$, for purely longitudinal perturbations, and in a constant shear, maximum growth rate was found at $|Ro^{(i)}| = 2$. This result may also be recovered by considering an exact solution of Euler's equations in terms of sheets of fluid moving independently (Métais et al. 1992).

The examination of the absolute vortex filaments (Figure 4) shows clearly that, during this stage, these are stretched in a hairpin manner and inclined approximately at 45° to the wall.

Fast rotation: $|Ro^{(i)}| = 0.1$. Because spanwise rotation has no effect on 2-D motions (without z dependence), the growth of the Tollmien–Schlichting waves (of streamwise wavelength $\lambda_x = 2\pi$) is unaffected. However, as opposed to the previous cases, the growth of the 3-D perturbations is totally inhibited. Consequently, the Tollmien–Schlichting waves remain stable and are able to reach a nonlinear saturated state. The flow is then composed of purely 2-D spanwise vortices of alternate sign vorticity on the different side of the channel (see Figure 5).

At small Rossby number, the flow exhibits several features in common with the 2-D channel simulations of Jiménez (1990). For instance, phenomena such as wall sweeps and ejections resulting from a chaotic behavior of the flow are present.

The full transition

Due to computer cost, the computation at $Re = 8000$ has to be stopped in the early stage of transition. Looser resolution can be used at lower Reynolds number and the full transition of the rotating channel can then be simulated. We here choose $Re = 3750$ and a smaller computational domain: $(L_x, L_y, L_z) = (2\pi, 2, \pi)$. The initial grid ($14 \times 129 \times 48$ resolution points) allows for the emergence of various modes. The final grid is $144 \times 129 \times 144$. The initial conditions are otherwise analogous to the previous section: two rotation rates are here considered

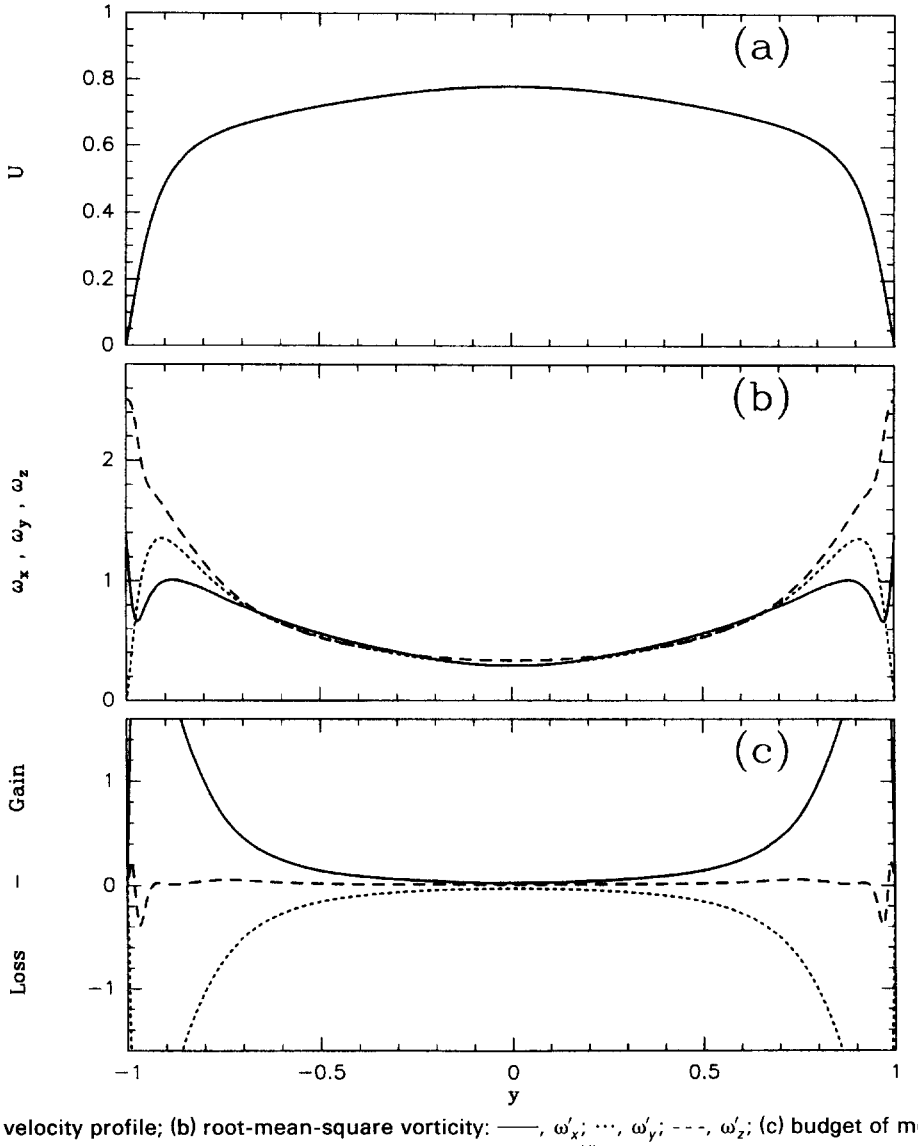

Figure 13 (a) Mean velocity profile; (b) root-mean-square vorticity: ——, ω'_x; ···, ω'_y; - - -, ω'_z; (c) budget of mean square vorticity $(1/2)\overline{\omega'^2}$: ——, stretching terms; ···, viscous terms; - - -, transport terms; ($|Ro^{(i)}| = \infty$, $Re = 3750$)

$|Ro^{(i)}| = 6$ and $|Ro^{(i)}| = 2$. Details related to the nonrotating case can be found in Gilbert and Kleiser (1990), Sandham and Kleiser (1992), and Zang and Krist (1989).

Figure 6 shows the time evolution of the fluctuating kinetic energy. It corresponds to the sum of the kinetic energy fluctuations in all spectral modes except the mean component. An integration is then performed over the whole y extend of the channel, and the result is normalized by the kinetic energy of the mean flow. After a short initial adjustment stage, the perturbation grows exponentially. As observed at higher Reynolds number (see preceding section), the growth is stronger for $|Ro^{(i)}| = 2$ than for $|Ro^{(i)}| = 6$.

By the time the perturbation has reached a finite amplitude, the nonlinear effects prevail. In this second stage, streamwise vortices form with a preferential spanwise spacing and then merge (see Alfredsson and Persson 1989; Yang and Kim 1991; Guo and Finlay 1991). Although the initial linear growth is stronger for $|Ro^{(i)}| = 2$ than for $|Ro^{(i)}| = 6$, the subsequent saturation level reached in the former case is lower than in the latter case.

The Reynolds number based upon the friction velocity is a good indicator of transition: it is given by the half width of the channel normalized by the friction velocity and is noted h^+. Figure 7 represents h_c^+ and h_a^+, respectively, estimated near the cyclonic and the anticyclonic walls. This clearly shows the strong asymmetry of the flow behavior near the two different walls: a rapid departure of h_a^+ from the laminar value is observed for $t \geq 15$ ($|Ro^{(i)}| = 2$) and for $t \geq 20$ ($|Ro^{(i)}| = 6$). Conversely, h_c^+ undergoes a slow raise before reaching a weak asymptotic value. This indicates a weak turbulence near the cyclonic wall, which could be a consequence of the strong turbulent events originated from the anticyclonic region.

Turbulent flow

We now compare the nonrotating and rotating turbulent flow in a channel at Re = 3750. The computational grid is $144 \times 129 \times 144$ for $|Ro^{(i)}| = \infty$ and $|Ro^{(i)}| = 6$ and $120 \times 129 \times 96$ for $|Ro^{(i)}| = 2$. The domain size is $(2\pi, 2, \pi)$ in the three cases. Dealiasing is applied in the two-spectral directions. The initial conditions

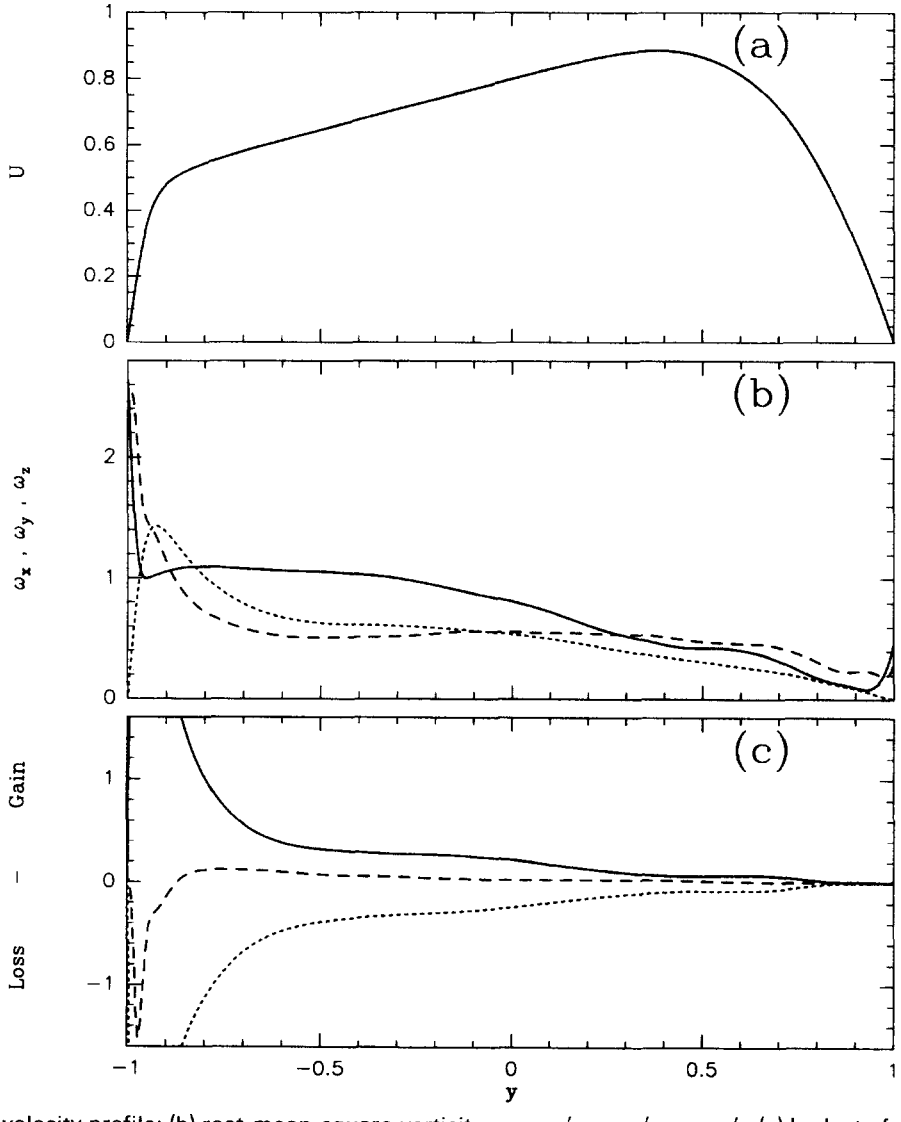

Figure 14 (a) Mean velocity profile; (b) root-mean-square vorticity: ——, ω'_x; ···, ω'_y; - - -, ω'_z; (c) budget of mean square vorticity $(1/2)\overline{\omega'^2}$: ——, stretching terms; ···, viscous terms; - - -, transport terms; ($|Ro^{(i)}| = 6$, Re = 3750)

consist in a field issued from a nonrotating calculation on which we impose a spanwise rotation. We then integrate until the flow reaches a statistically steady state. Let us note that this procedure provides a turbulent stage which is statistically identical with the final stage of the full transition described in the preceding section. For the two rotation regimes here considered, the turbulence intensity is higher on the anticyclonic side than on the cyclonic side where relaminarization occurs. We have checked that the statistical results such as those shown in Figure 8 agree well with the simulations performed by Kristoffersen and Andersson (1993).

We have used a higher resolution than Kristoffersen and Andersson (1993) in order to be able to precisely investigate the coherent structures embedded within the flow. Particularly, we examine how the instantaneous vorticity field differs from the nonrotating case. Comparison of the isosurface of the relative vorticity modulus $\omega = 3$ or 2 (Figures 9–11) clearly shows a change of vortex topology when rotation is applied. Near the cyclonic wall, the isovorticity surfaces are nearly flat, indicating a weak growth of the perturbation. On the anticyclonic side, the modification of the turbulence level is associated with the longitudinal vorticity intensification.

Next we examine the distribution of the angle $\theta = \tan^{-1}(\omega_y/\omega_x)$. It represents the inclination angle of the projection on the (x, y)-plane of the (absolute or relative) vorticity vector with respect to the wall. We here follow the procedure developed by Moin and Kim (1985). Each contribution to the distribution is weighted by the magnitude of the vorticity projection. We here consider a flow region far from the wall corresponding to $y = -0.5$. At this location, the distribution differs appreciably in the nonrotating and rotating cases (Figure 12): in the nonrotating case, the histogram for θ presents a peak around 45°, in agreement with Moin and Kim. For $|\mathrm{Ro}^{(i)}| = 6$, the anticyclonic region is mainly composed of vortex lines inclined at $\approx 25°$, while for $|\mathrm{Ro}^{(i)}| = 2$, the most probable angle is around 10°. The sharper peak is observed in the latter case, indicating a very pronounced flow organization. Superposed on these structures, we also observe for $|\mathrm{Ro}^{(i)}| = 6$ large-scale longitudinal rolls (Taylor–Görtler-like vortices) as in the laboratory experiments of Johnston et al. (1972) and the direct numerical simulations of Kristoffersen and Andersson (1993). For $|\mathrm{Ro}^{(i)}| = 2$, these large-scale rolls do not seem to be present.

The mean velocity profile exhibits a characteristic linear region of slope 2Ω (see Figures 14a, 15a). It is associated with a

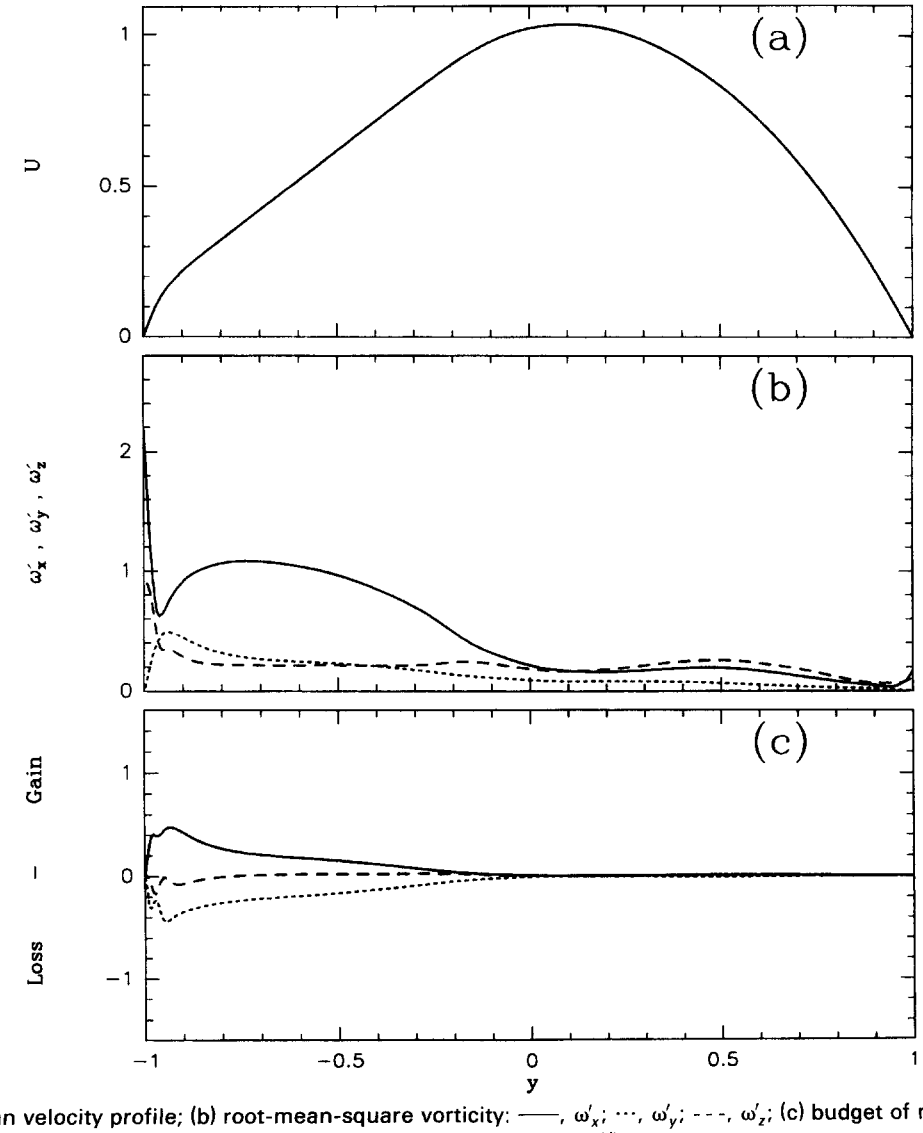

Figure 15 (a) Mean velocity profile; (b) root-mean-square vorticity: ——, ω'_x; ···, ω'_y; - - -, ω'_z; (c) budget of mean square vorticity $(1/2)\overline{\omega'^2}$: ——, stretching terms; ···, viscous terms; - - -, transport terms; ($|\mathrm{Ro}^{(i)}| = 2$, $\mathrm{Re} = 3750$)

local Rossby number $\mathrm{Ro}(y) = -1$ (see Equation 1). As suggested by the phenomenological theory of Lesieur et al. (1991), in such a range of near-zero absolute spanwise vorticity, the production of longitudinal vorticity should be favored. Figures 13b, 14b, and 15b compare the rms of the fluctuating vorticity components at $|\mathrm{Ro}^{(i)}| = \infty$, $|\mathrm{Ro}^{(i)}| = 6$, and $|\mathrm{Ro}^{(i)}| = 2$. In the rotating case, the longitudinal component reaches a plateau within the $\mathrm{Ro}(y) = -1$ region and largely exceeds the other two components. This seems to confirm the predictions of Lesieur et al. (1991).

However, regions of local Rossby number of -1 can also be viewed as neutral stability regions (Ferziger et al. 1976; Tritton 1992). In the latter, one could be inclined to think that the turbulence activity principally results from the convection by the large-scale vortices of the highly turbulent fluid originally situated near the anticyclonic wall. To answer this question, we have examined the various terms of the transport equations for the mean square of the fluctuating vorticity components. These equations are given (Tennekes and Lumley 1972) by

$$\frac{D}{Dt}\left(\frac{\overline{\omega_i'\omega_i'}}{2}\right) = T_{ii} + S_{ii} + V_{ii} \tag{4}$$

$$T_{ii} = -\overline{u_j'\omega_i'}\,\overline{\omega}_{ai,j} - \tfrac{1}{2}(\overline{u_j'\omega_i'\omega_i'})_{,j}$$

$$S_{ii} = \overline{\omega_i'\omega_j'u_{i,j}'} + \overline{\omega_i'\omega_j'}\,\overline{u}_{i,j} + \overline{\omega}_{aj}\overline{\omega_i'u_{i,j}'}$$

$$V_{ii} = \tfrac{1}{2}\nu(\overline{\omega_i'\omega_i'})_{,jj} - \nu\overline{\omega_{i,j}'\omega_{i,j}'} \tag{5}$$

T_{ii}, S_{ii}, and V_{ii} respectively represent the sum of the stretching terms, transport terms (production + turbulent transport), and viscous terms (diffusion + dissipation). The indices $(1,2,3)$ are used to denote the (x, y, z) directions. $(\overline{u}_i, u_i')$ and $(\overline{\omega}_{ai}, \omega_i')$ are, respectively, the mean value and the fluctuation of velocity and absolute vorticity. An overbar indicates an average over x, z, and t. We have checked that, in the nonrotating case, each $(1/2)\overline{\omega_i'\omega_i'}$ budget is in good agreement with those of Antonia and Kim (1994). We present here the budget of $(1/2)\overline{\omega'^2} = (1/2)(\overline{\omega_1'\omega_1'} + \overline{\omega_2'\omega_2'} + \overline{\omega_3'\omega_3'})$ for $|\mathrm{Ro}^{(i)}| = \infty, 6, 2$, and our analysis concerns only the region far from the wall. The study of the rotation effects on the near-wall regions will be the subject of a future work. The stretching term exhibits a plateau in the region of zero spanwise absolute vorticity corresponding to $y \leq 0$, and clearly prevails over the transport term (see Figures 14c, 15c). This shows that an intense stretching of absolute vorticity takes place in agreement with the phenomenological arguments proposed by Lesieur et al. (1991). The stretching term decreases for $y > 0$ and becomes very small near the cyclonic wall confirming the inhibition of vortex stretching in this region.

Conclusion

We have presented 3-D direct numerical simulations of the transitional and turbulent rotating channel flow using highly accurate numerical schemes. This has allowed us to perform a detailed investigation of the vortices embedded within the flow. In the transitional case and for rapid rotation, the growth of the three-dimensionality is totally inhibited and the flow eventually consists in large-scale 2-D vortices parallel to the rotation axis. These result from the growth and saturation of the energy of the Tollmien–Schlichting waves. Conversely, a rapid transition toward fully developed 3-D turbulence is observed on the anticyclonic side of the channel when moderate rotation is applied. This is attributable to the rapid amplification of modes of zero or near-zero longitudinal component. At moderate rotation ($|\mathrm{Ro}^{(i)}| = 6$ and $|\mathrm{Ro}^{(i)}| = 2$), we observe, in the turbulent regime, the development, over a large portion of the channel width, of a well-defined region in which the mean absolute vorticity is close to zero. In this region, the flow is composed of hairpin vortices of weak inclination with respect to the wall (up to 10° for $|\mathrm{Ro}^{(i)}| = 2$). Furthermore, the analysis of the different terms involved in the equations for the mean square (absolute) vorticity fluctuations shows that the stretching mechanisms play a major role. These are much more important than the transport processes.

Acknowledgments

We are grateful to Joel H. Ferziger for helpful comments on this work, Pierre Comte, and Jorge Silvestrini for informative discussions. Computations were carried out at the IDRIS (Institut du Développement et des Ressources en Informatique Scientifique, Paris).

References

Alfredsson, P. H. and Persson, H. 1989. Instabilities in channel flow with system rotation, *J. Fluid Mech.*, **202**, 543–557

Antonia, R. A. and Kim, J. 1994. Low-Reynolds-number effects on near-wall turbulence. *J. Fluid Mech.*, **276**, 61–80

Ferziger, J. H. and Shaanan, S. 1976. Effect of anisotropy and rotation on turbulence production. *Phys. Fluids*, **19**, 596–597

Finlay, W. H. 1990. Transition to oscillatory motion in rotating channel flow. *J. Fluid Mech.*, **215**, 209–227

Finlay, W. H. 1992. Transition to turbulence in a rotation channel. 1992 *J. Fluid Mech.*, **237**, 73–99

Gilbert, N. and Kleiser, L. 1990. Near-wall phenomena in transition to turbulence. In *Near-Wall Turbulence*, S. J. Kline and N. H. Afgan (eds.), Hemisphere, Bristol, PA, 7–27

Guo, Y. and Finlay, W. H. 1991. Splitting, merging, and wavelength selection of vortices in curved and/or rotating channel flow due to Eckhaus instability. *J. Fluid Mech.*, **228**, 661–691

Jiménez, J. 1990. Transition to turbulence in two-dimensional Poiseuille flow. *J. Fluid Mech.*, **218**, 265–297

Johnston, J. P., Halleen, R. M. and Lezius, D. K. 1972. Effects of spanwise rotation on the structure of two-dimensional fully developed turbulent channel flow. *J. Fluid Mech.*, **56**, 533–557

Kim, J. 1983. The effect of rotation on turbulence structure. In *Proc. of the 4th Symposium on Turbulent Shear Flows*, Karlsruhe, Germany, 6.14–6.19

Kim, J., Moin, P. and Moser, R. 1987. Turbulence statistics in fully developed channel flow at low Reynolds number. *J. Fluid Mech.*, **177**, 133–166

Kim, J. and Moser, R. D. 1989. On the secondary instability in plane Poiseuille flow. *Phys. Fluids A*, **1**, 775–777

Kristoffersen, R. and Andersson, H. I. 1993. Direct simulations of low-Reynolds-number turbulent flow in a rotating channel. *J. Fluid Mech.*, **256**, 163–197

Lele, S. K. 1992. Compact finite difference schemes with spectral-like resolution, *J. Comput. Phys.*, **103**, 16–42

Lesieur, M., Yanase, S. and Métais, O. 1991. Stabilizing and destabilizing effects of a solid-body rotation on quasi-two-dimensional shear layers. *Phys. Fluids A*, **3**, 403–407

Métais, O., Flores, C., Yanase, S., Riley, J. J. and Lesieur, M. 1995. Rotating free shear flows Part 2: Numerical simulations. *J. Fluid Mech.*, **293**, 41–80

Métais, O., Yanase, S., Flores, C., Bartello, P. and Lesieur, M. 1992. Reorganization of coherent vortices in shear layers under the action of solid-body rotation. In *Turbulent Shear Flows VIII*, Springer, New York, 415–430

Moin, P. and Kim, J. 1985. The structure of the vorticity field in turbulent channel flow. Part 1. Analysis of instantaneous fields and statistical correlations. *J. Fluid Mech.*, **155**, 144–464

Piomelli, U. and Liu, J. 1995. Large-eddy simulation of rotating channel flows using a localized dynamic model. *Phys. Fluids*, **7**, 839–848

Sandham, N. D. and Kleiser, L. 1992. The late stages of transition to turbulence in channel flow. *J. Fluid Mech.*, **245**, 319–348

Shih, T. M., Tan, C. H. and Hwang, B. C. 1989. Effects of grid staggering on numerical schemes. *Int. J. Numer. Methods Fluids*, **9**, 193–212

Tafti, D. K. and Vanka, S. P. 1991. A numerical study of the effects of spanwise rotation on turbulent channel flow. *Phys. Fluids A*, **3**, 642–656

Tennekes, H. and Lumley, J. L. 1972. *A first Course in Turbulence*. MIT Press, Cambridge, MA

Tritton, D. J. 1992. Stabilization and destabilization of turbulent shear flow in a rotating fluid. *J. Fluid Mech.*, **241**, 503–523

Yanase, S., Flores, C., Métais, O. and Riley, J. 1993. Rotating free-shear flows. I. Linear stability analysis. *Phys. Fluids A*, **5**, 2725–2737

Yang, K. S. and Kim, J. 1991. Numerical investigation of instability and transition in rotating plane Poiseuille flow. *Phys. Fluids A* **3**, 633–641

Zang, T. A. and Krist, S. E. 1989. Numerical experiments on stability and transition in plane channel flow. *Theoret. Comput. Fluid Dynamics*, **1**, 41–64